Program Digest, 2019 IEEE International Ultrasonics Symposium (IUS)
Glasgow, Scotland, October 6-9, 2019

Efficient Angle Selection for Coherent Plane Wave Compounding

Haroon Ali Akbar
General Motors Canada
Oshawa, Canada
haroonaliakbar@uvic.ca

Daler Rakhmatov
University of Victoria
Victoria, Canada
daler@ece.uvic.ca

***Abstract*—Ultrasound imaging based on multiple steered plane-wave emissions and coherent compounding can achieve very high frame rates, thus enabling the user to obtain valuable information about blood flow or tissue motion characteristics. After emitting a plane wave at some angle, a transducer array records returning echoes that are subsequently processed to form an individual image dataset. Several plane-wave emissions at different angles yield multiple image datasets that can be coherently compounded to improve the final image quality. We propose an efficient method for selecting a reduced subset of plane-wave emission angles, which lowers the data acquisition cost while still producing good-quality images. Our angle-selection scheme relies on a similarity-driven recursive search within the user-specified angular range.**

***Index Terms*—Plane-wave ultrasound imaging, coherent compounding, reduced data acquisition**

I. Introduction

Ultrafast plane-wave (PW) ultrasound imaging [1] typically involves the following basic steps: 1) insonifying the medium with several PW pulses emitted at different steering angles, 2) sampling the backscattered signals after each PW emission, 3) beamforming each angle-specific raw data frame acquired, 4) coherently compounding the resulting beamformed data frames over all angles, and 5) post-processing the compounded data frame (e.g., envelope detection and log-compression to obtain a B-mode image). Using fewer PW emission angles means acquiring and beamforming fewer raw data frames, which translates into savings in terms of data sampling and processing, but it may also adversely affect the resulting image quality.

We aim to address the following question: Given a set of N available PW emission angles θ_1 (smallest), θ_2, ..., θ_N (largest), which ones should we choose (i.e., which angle-specific raw data frames should we acquire and beamform) to get good-quality compounded images at a reduced cost? We propose a simple angle-selection method guided by beamformed data similarity measurements. Unlike [2], where the number of PW emissions was reduced by using a convolutional neural network (trained for compounding), our approach does not require any additional training/validation datasets.

This work was supported in part by the Natural Sciences and Engineering Research Council of Canada (NSERC).

II. Proposed Method

Our objective is to determine a subset S of angle indices n among $1, 2, ..., N$, which implies acquiring 2D raw data frames RF$[n]$ and computing their respective beamformed data frames BF$[n]$; summing the latter over the indices in S would yield the final compounded frame. Fig. 1 shows our proposed *recursive scheme* for generating S based on a similarity-driven search.

We start with $S = \{1, N\}$, i.e., the raw data frames RF$[1]$ and RF$[N]$ for θ_1 (the smallest angle) and θ_N (the largest angle) have already been acquired, and the corresponding beamformed data frames BF$[1]$ and BF$[N]$ are available. After initializing the left/right boundary indices ($l = 1$ and $r = N$), we are ready to call our angle-selection function SIMSEARCH shown in Fig. 1.

```
function [BF, S] ← SimSearch(RF, BF, T, S, l, r) {
Let n ← ⌊(l + r)/2⌋;
if n ∉ S then {
  Let S ← S ∪ {n} and acquire RF[n];
  Compute BF[n] ← Beamform(RF[n]);
  Let U ← (|BF[l]| + |BF[n]| + |BF[r]|)/3;
  Compute L̄ ← Similarity(U, (|BF[n]| + |BF[r]|)/2);
  Compute R̄ ← Similarity(U, (|BF[l]| + |BF[n]|)/2);
  if L̄ < T then [BF, S] ← SimSearch(RF, BF, T, S, l, n);
  if R̄ < T then [BF, S] ← SimSearch(RF, BF, T, S, n, r);
}}
```

Fig. 1. Similarity-driven recursive search function SIMSEARCH.

We choose the $[l, r]$ interval midpoint $n = \lfloor (l+r)/2 \rfloor$ next, which corresponds to a PW emission at θ_n and the subsequent acquisition of RF$[n]$, provided that S does not already contain index n. We proceed to compute BF$[n]$ and a pointwise-averaged data frame $U = (|\text{BF}[l]| + |\text{BF}[n]| + |\text{BF}[r]|)/3$, using the absolute values of beamformed data points obtained for PW emissions at angles θ_l, θ_r, and θ_n.[1] Then, we assess the relative significance of BF$[l]$ by measuring the similarity indicator $\overline{L}$ between U (including BF$[l]$) and $(|\text{BF}[n]| + |\text{BF}[r]|)/2$ that excludes BF$[l]$; we also assess the relative significance of BF$[r]$ by measuring the similarity indicator $\overline{R}$ between U and $(|\text{BF}[l]| + |\text{BF}[n]|)/2$. If $\overline{L}$ is below some similarity

[1] To obtain a (j, k)-element of matrix U (i.e., a data value stored in row j and column k), we simply average the absolute values of the (j, k)-elements from matrices BF$[l]$, BF$[r]$, and BF$[n]$, which can be interpreted as computing a normalized ℓ_1-norm of a three-element vector.

threshold T, our SIMSEARCH function calls itself to explore the left half-interval $[l, n]$. Intuitively, having $\overline{L} < T$ suggests that the contribution of BF$[l]$ to U was relatively significant, containing enough "dissimilar information" to warrant using an additional PW emission at an angle between θ_l and θ_n. The right half-interval $[n, r]$ is explored when $\overline{R} < T$. Upon completion of such similarity-driven search, we will have a collection of beamformed data frames BF$[n \in S]$ to undergo coherent compounding and further post-processing.

III. Evaluation Results

Our evaluation results are based on three PICMUS-2017 experimental datasets [3] that utilize $N = 75$ PW emission angles, ranging from $\theta_1 = -16°$ to $\theta_{75} = +16°$. Fig. 2 shows the fully compounded B-mode images designated as TYPE-1, TYPE-2, and TYPE-3. These full-acquisition (75 PWs) *baseline* images have been obtained using the default IQ delay-and-sum (DAS) beamformer from [3]. Table I summarizes their respective image quality metrics, including the contrast-to-noise ratio (CNR), full-width at half-maximum (FWHM), and resolution measurements that have been calculated using the original evaluation routines from [3].[2] For the TYPE-1 images, Table I reports the CNR values for the top/bottom cyst phantoms (anechoic cylinder targets) and the axial/lateral FWHM values for the bottom-right point phantom (a wire target). For the TYPE-2 images, Table I reports the axial/lateral FWHM values averaged over the shown (seven) point phantoms. For the TYPE-3 images, Table I reports the axial/lateral FWHM values for the leftmost and off-center bottom point phantoms (labeled FWHM$_1$ and FWHM$_2$, respectively), as well as the axial/lateral distances measured between progressively closer pairs of neighboring point phantoms in the displayed cluster.

We have tested two variants of our angle selection scheme, using the mean-squared error (MSE) and structural similarity index measurements (SSIM) [4] as two alternative indicators of beamformed data similarity. We have employed the same PICMUS-provided IQ DAS beamformer producing complex-valued BF$[\cdot]$ frames. To reduce overhead, we have replaced $|$BF$[\cdot]|$ with the absolute values of the real part only.

Fig. 2 shows the compounded B-mode images resulting from the SSIM-driven search (i.e., checking for $\overline{L}_{\text{SSIM}} < T$ and $\overline{R}_{\text{SSIM}} < T$), and Fig. 3 shows the results for the MSE case (i.e., checking for $\overline{L}_{\text{MSE}} > T$ and $\overline{R}_{\text{MSE}} > T$). The threshold T can be specified by the user, or its values can be automatically determined after processing extra initial raw data frames for angles θ_2 and θ_{74} (i.e., in addition to initial θ_1 and θ_{75}). Letting $V = (|\text{BF}[1]| + |\text{BF}[2]|)/2$ and $W = (|\text{BF}[74]| + |\text{BF}[75]|)/2$, we have set our thresholds as follows (see Fig. 3 and 4):

$$T_{\text{SSIM}} = \max\{\text{SSIM}(V, |\text{BF}[1]|), \text{SSIM}(W, |\text{BF}[75]|)\},$$

$$T_{\text{MSE}} = \min\{\text{MSE}(V, |\text{BF}[1]|), \text{MSE}(W, |\text{BF}[75]|)\}.$$

Table I lists the corresponding image quality metrics for the SSIM- and MSE-based acquisition scenarios, next to the full-acquisition baseline. In terms of resolution and axial FWHM, all three scenarios offer practically the same performance. When using our proposed scheme, the CNR values become slightly worse, while the lateral FWHM values become slightly better, compared to the full-acquisition case. These results indicate that our angle-selection method (generating only 13-19 PW emissions) yields compounded images that are comparable in quality to those obtained using all 75 PW emissions. One promising direction for future research would be to investigate more sophisticated similarity thresholding (e.g., with region-of-interest restrictions) coupled with faster alternatives to DAS beamforming [5].

[2]We also note that the presented images have passed all the geometric distortion tests and Kolmogorov-Smirnov tests for speckle preservation [3].

TABLE I
COMPOUNDED B-MODE IMAGE QUALITY METRICS.

TYPE-1 Image Quality Metric	Full Acq. (75 PWs)	SSIM Acq. (18 PWs)	MSE Acq. (19 PWs)
CNR_{top} (dB)	13.2	12.8	12.9
$\text{CNR}_{\text{bottom}}$ (dB)	12.2	11.9	11.9
Axial FWHM (mm)	0.48	0.49	0.49
Lateral FWHM (mm)	0.64	0.60	0.61

TYPE-2 Image Quality Metric	Full Acq. (75 PWs)	SSIM Acq. (15 PWs)	MSE Acq. (19 PWs)
Axial FWHM_{ave} (mm)	0.48	0.48	0.48
Lateral FWHM_{ave} (mm)	0.62	0.57	0.57

TYPE-3 Image Quality Metric	Full Acq. (75 PWs)	SSIM Acq. (13 PWs)	MSE Acq. (19 PWs)
Axial FWHM_1 (mm)	0.47	0.47	0.47
Lateral FWHM_1 (mm)	0.72	0.71	0.70
Axial FWHM_2 (mm)	0.48	0.49	0.48
Lateral FWHM_2 (mm)	0.62	0.60	0.58
Axial Resolution (Distance, mm)	3.86	3.87	3.87
	2.90	2.90	2.90
	1.99	1.98	1.99
	1.04	1.03	1.03
	0.63	0.62	0.62
Lateral Resolution (Distance, mm)	4.07	4.07	4.07
	3.15	3.16	3.16
	2.14	2.14	2.15
	1.10	1.10	1.11
	—	0.73	0.74

References

[1] G. Montaldo, M. Tanter, J. Bercoff, N. Benech, and M. Fink, "Coherent plane-wave compounding for very high frame rate ultrasonography and transient elastography," *IEEE Trans. Ultrason., Ferroelect., Freq. Contr.*, vol. 56, no. 3, pp. 489–506, Mar 2009.

[2] M. Gasse, F. Millioz, E. Roux, D. Garcia, H. Liebgott, and D. Friboulet, "High-quality plane wave compounding using convolutional neural networks," *IEEE Trans. Ultrason., Ferroelect., Freq. Contr.*, vol. 64, no. 10, pp. 1637–1639, Oct 2017.

[3] CREATIS, "Plane-wave Imaging Challenge in Medical UltraSound (PICMUS): Algorithm Evaluation Framework." [Online]. Available: https://www.creatis.insa-lyon.fr/EvaluationPlatform/picmus/

[4] Z. Wang, A. Bovik, H. Sheikh, and E. Simonchelli, "Image quality assessment: from error visibility to structural similarity," *IEEE Trans. Image Processing*, vol. 13, no. 4, pp. 600–612, Apr 2004.

[5] M. Albulayli and D. Rakhmatov, "Fourier-domain depth migration for plane wave ultrasound imaging," *IEEE Trans. Ultrason., Ferroelect., Freq. Contr.*, vol. 65, no. 8, pp. 1321–1333, Aug 2018.

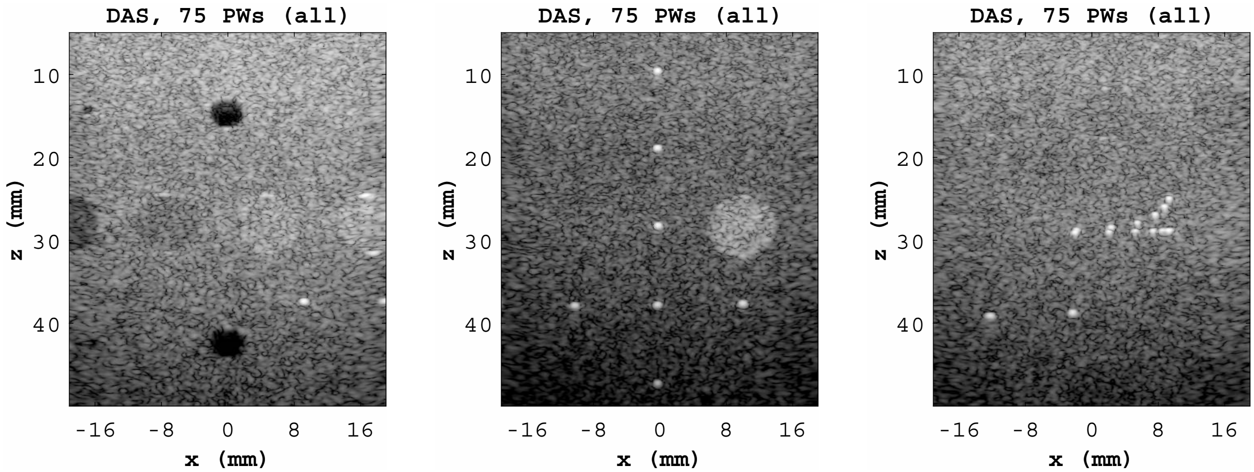

Fig. 2. From left to right: TYPE-1, TYPE-2, and TYPE-3 baseline images obtained using all 75 plane-wave emissions [3].

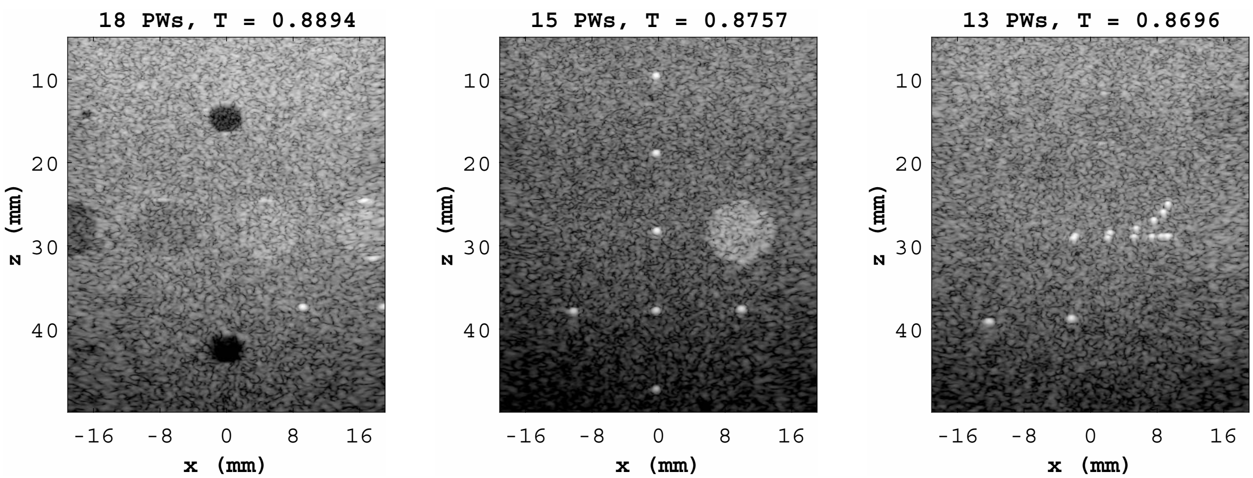

Fig. 3. From left to right: TYPE-1, TYPE-2, and TYPE-3 compounded images obtained using SSIM-driven angle selection.

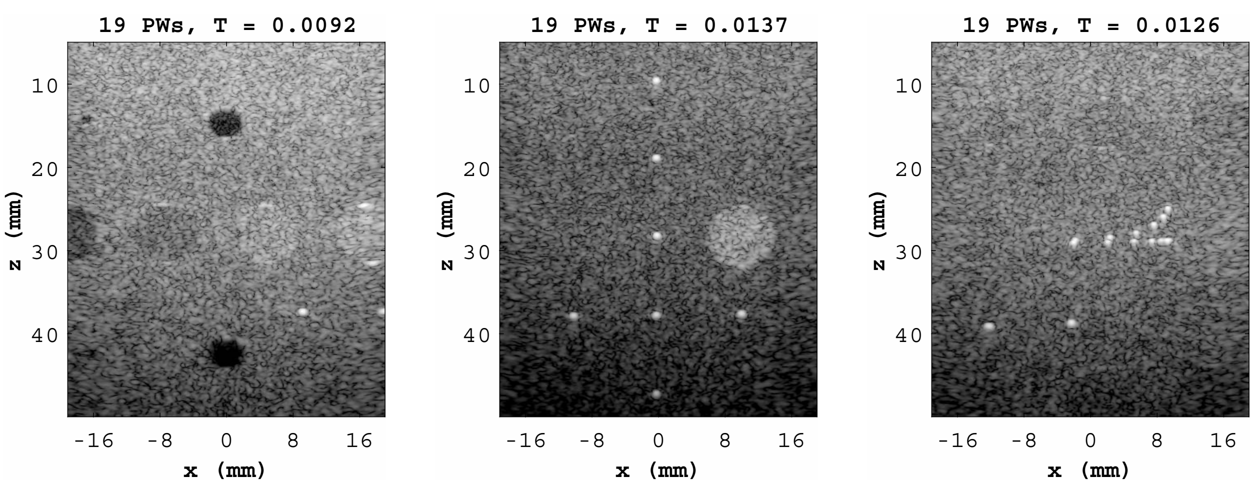

Fig. 4. From left to right: TYPE-1, TYPE-2, and TYPE-3 compounded images obtained using MSE-driven angle selection.